Energy Storage Materials 55 (2023) 42–54

Contents lists available at ScienceDirect

Energy Storage Materials

journal homepage: www.elsevier.com/locate/ensm

Opening twisted polymer chains for simultaneously high printability and battery fast-charge

Ying Wang [a,1], Jinlong He [b,1], Daxian Cao [a], Ercan Cakmak [c], Xianhui Zhao [c], Qingliu Wu [d], Yuyue Zhao [a], Haoze Ren [a], Xiao Sun [a], Ying Li [b], Hongli Zhu [a,*]

[a] Department of Mechanical and Industrial Engineering, Northeastern University, Boston, MA 02115, USA
[b] Department of Mechanical Engineering, University of Wisconsin-Madison, Madison, WI 53706 - 1572, USA
[c] Manufacturing Science Division, Oak Ridge National Laboratory, Oak Ridge, TN 37831, USA
[d] Department of Chemical and Paper Engineering, Western Michigan University, Kalamazoo, MI 49008, USA

ARTICLE INFO

Keywords:
Ink preparation
Screen printing
Printability
Polymer chains
Lattice Boltzmann method

ABSTRACT

Fast-charging is key to the widespread adoption of battery-based electric vehicles. However, improving fast-charging through architecture optimization is expensive. To reduce costs and expand to commercialization, we applied roll-to-roll screen printing technology to create channels and decrease the tortuosity of electrodes. For the first time, this work successfully opened twisted polymer chains within high-solid-content inks to improve their screen printability and battery performance of as-printed electrodes. With $LiNi_{0.6}Mn_{0.2}Co_{0.2}O_2$ as active materials, the 60% solid content ink presents superior screen printability after opening the twisted binder chains. As-printed electrode exhibits 33% higher charge capacity at 6 C than printed electrode with chains twisted ink at mass loading of 6.5 mg/cm^2. Furthermore, coarse-grained molecular dynamics simulations are performed to study the underlying mechanism systematically. The new ink preparation procedure provides a scalable, effective strategy for manufacturing screen-printable battery ink and promotes screen-printed electrode technology.

1. Introduction

The widespread adoption of electric vehicles has promoted extensive research on technologies for fast-charging lithium-ion (Li-ion) batteries. In addition to investigating new electrode materials and novel battery chemistries, reducing the tortuosity of electrodes is a widely accepted strategy to enhance the fast-charge capacity since the low-tortuosity structure can enhance electrolyte mass transfer and shorten Li-ion diffusion [1,2]. Currently, three strategies can be used to achieve low-tortuosity electrodes: (1) fabricating channels through the accumulation of oriented pores, which are generated with chemical, mechanical, and physical methods through sacrificial phases [3–5]; (2) directly producing aligned electrodes with physical or mechanical methods, such as magnetic field application [6], extrusion [7], and directional freeze drying; [8] and (3) active loading materials on an aligned template, such as carbonized wood [9], aligned carbon fibers [10], or aligned carbonized viruses [11]. Although the above methods established aligned channels within electrodes, reduced ortuosity of electrodes, and improved their fast-charging capacity, most methods are limited to the laboratory demonstration scale and not yet commercially viable due to their complexity, low productivity, high cost, and limited producible size.

People started using printing technology more than 2000 years ago, and industrial roll-to-roll (R2R) printing has been widely used in manufacturing commercial books, magazines, and newspapers for about two centuries. Because of its many advantages, including the facile process, no added impurities, high output, low cost, and large sample fabricability, R2R printing was recently introduced into batteries [12,13]. Compared with the traditional bar coating technology to manufacture electrodes, R2R printing offers unique benefits in electrode preparation, including integrating patterns, establishing functional electrode architectures, and extending to large-scale industrial low-tortuosity electrode fabrication. As a typical R2R printing technique [14], R2R screen printing renders high ink transfer per printing layer. While screen printing has been introduced in battery and capacitor investigations [15], no research has attempted to apply screen printing to design electrodes with low-tortuosity three-dimensional architectures for fast-charging devices.

* Corresponding author.
E-mail address: h.zhu@neu.edu (H. Zhu).
[1] These authors contributed equally to this work

https://doi.org/10.1016/j.ensm.2022.11.025
Received 9 May 2022; Received in revised form 6 October 2022; Accepted 13 November 2022
Available online 15 November 2022

Despite having many benefits, the R2R printing battery technology is limited to low mass loading per printing layer. The amount of loading per printing layer is highly dependent on the solid content of the inks. For example, low solid content of 40% leads to a low mass loading of 0.4 mg/cm^2 for single-layer screen printing [16], whereas a relatively high solid content of 60% leads to a high areal mass loading of 2.2 mg/cm^2 per printing layer in this work. Moreover, high-solid-content inks consume less solvent during ink preparation and less energy during drying than low-solid-content inks. Although ink with high solid content is necessary for the industrialization of screen-printed batteries, the high solid content can negatively impair the rheological properties and screen printability of inks. Unfortunately, few studies on the formula-property-printability relationship have been reported, and to date, most screen-printable Li-ion cathode inks have a solid content below 40 wt.% [17–20]. This solid content is much lower than that of electrode slurries used for traditional bar-coating manufacturing processes (greater than 55%) [21]

In addition, as an indispensable component in electrode inks, the binder influences both the ink printability and the electrode micromorphology and therefore affects the electrochemical performance of as-printed electrodes. Previous works have indicated that both the weight content and number average molecular weight (Mn) of the binder play a critical role in screen printing [22,23]. Specifically, raising the weight content and selecting a high-Mn binder enhances the connectivity between components within inks, but it can impair the screen printability of inks [24]. Concurrently, inks with highly twisted molecular chains exhibit poor thixotropic properties and screen printability [25]. Beyond its significant influence on screen printability, the binder is critical to the electrochemical performances of as-printed electrodes. As an electrode component, the binder connects the different components within the electrode as well as the electrode and current collector, providing mechanical stability for the electrode and therefore improving the electrochemical cycling stability [26]. However, the excessive binder can impede the transport of electrons and ions in the electrode and thus negatively affects the rate performance. Therefore, the exploration and optimization of binders are necessary to reach both excellent printability under a high solid content and elevated battery performance [27].

In this work, for the first time, we report the effect of the molecular chain status (twisted or untwisted) within inks on the rheological properties and screen printability of inks produced through three different ink preparation methods. We further investigated the influence of the screen printability of inks on the structure of screen-printed electrodes via X-ray computed tomography (XCT). Additionally, the electrochemical properties of screen-printed electrodes were analyzed to reveal the underlying material-structure-property-performance relationships among the molecular chain status, ink dynamic viscosity, and screen printability of inks, as well as micromorphology and electrochemical performance of screen-printed electrodes. Ultimately, an optimized ink preparation procedure was developed to achieve excellent screen-printable inks with untwisted molecular chains while ensuring homogeneous dispersion of the components at a high solid content (60%). Results show that the innovative ink preparation procedure can dramatically improve the performances of the screen-printed electrodes in the rate and long-term cycling. In addition, coarse-grained molecular dynamics (CGMD) are performed to investigate the underlying mechanisms at the micro-level since it is computationally more effective and enables the studied simulation system to have much longer time scales and larger size scales. Through CGMD simulations, we reveal the relationships between different ink preparation procedures and performance metrics, including shear behaviors, ink component distribution, and fluidity during the printing process. Overall, this work developed an optimal ink preparation methodology to ensure both excellent screen printability and high battery performance, which paves the way toward the industrial manufacturing of low-tortuosity electrodes through screen printing for fast-charging.

2. Results and discussion

Uniformly squeezing ink through a mesh and transferring it onto a substrate is essential to reach outstanding screen printability. The binder within inks significantly affects the rheological properties and, therefore, the screen printability of the ink. Especially under a high ink solid content, the long polymer chains of the binder are physically entangled and twisted, thereby increasing the ink viscosity and reducing the screen printability. To achieve excellent printability, herein, we investigated three ink preparation procedures and developed an approach to open twisted polymer chains. As intuitively shown in Figs. 1(A1) and 1(A2), we first exhibit the relationship between the screen printability of inks with twisted and untwisted molecular chains, respectively. Twisted molecular chains act as additional nets, wrapping and pulling on the ink particles, hindering them from passing through the mesh of the screen. In the opposite situation, the molecular chains within the ink are untwisted. In this case, an equivalent amount of particles and polymer chains as in the previous case form an opened and well-dispersed ink. These well-dispersed units can be effortlessly transferred to the substrate through the mesh during screen printing.

Based on the above-discussed relationship between the molecular chain status of the binder within the ink and the resulting screen printability, we designed a novel and straightforward procedure to prepare the screen-printable electrode ink, named the two-step approach. Fig. 1(B1–B4) exhibit the preparation process of the two-step approach and the corresponding micromorphological feature within the ink. A certain amount of solvent is separately added in two separate steps: (1) the first part of the solvent is added with the conductive additive to adequately disperse the components within the ink, and (2) the second part of the solvent is introduced after the binder has been mixed to open the twisted molecular chains and obtain a low viscosity at a high solid content. The disentangled and liberated binder endows the ink with low viscosity and outstanding screen printability.

To demonstrate the effects of the molecular chain status on the rheological properties and screen printability, we prepared 60% solid content inks with various molecular chain statuses containing $LiNi_{0.6}Mn_{0.2}Co_{0.2}O_2$ (NMC 622) (active material), super P (conductive additive), polyvinylidene fluoride (PVDF, binder), and 1-methyl-2-pyrrolidone (NMP, solvent). Specifically, ink was prepared by Method 1 (M1), corresponding to the traditional method, i.e., dispersing super P, adding NMC 622, and mixing the binder solution; the ink was produced by Method 2 (M2), matching the most commonly used method in the laboratory, i.e., mixing all components; and ink was fabricated by Method 3 (M3) corresponding the two-step approach mentioned above, separating the solvent (NMP) into two parts and adding the parts separately. As mentioned above, the M1 and M2 inks are twisted molecular chain inks (named “T-Inks”) since the binder solution is added at the end and creates additional nets. In contrast, the M3 ink is an untwisted molecular chain ink (named “U-Ink”). The corresponding mixing processes and optical images of the mixtures in each step are detailed in Fig. S1. Although all three inks are macroscopically homogeneous, their internal micromorphological structure needed to be elucidated through rheological property evaluation.

Rheological studies were carried out to study the flow behaviors and thixotropy of the M1, M2, and M3 inks. The viscosity–shear rate plots show that all inks exhibit shear-thinning behavior, as presented in Fig. 2 (A). The viscosities of all inks decrease as the shear rate increases and remain below 10 Pa·s when the shear rate is higher than 10 s^{-1}, which is in the proven screen a printable range of 1–10 Pa·s [28]. Furthermore, the viscosities of the M1, M2, and M3 inks are in decreasing order, and the viscosity differences among the inks are more pronounced at low shear rates. The strongest interaction among components within the M1 ink contributes to the force between the heavily intertwined molecular chains. This force is further reflected in the fact that the M1 ink has a yield shear stress approximately twice that of the M2 and M3 inks, as displayed in Fig. 2(B). Therefore, although M2 ink is T-ink, its molecular

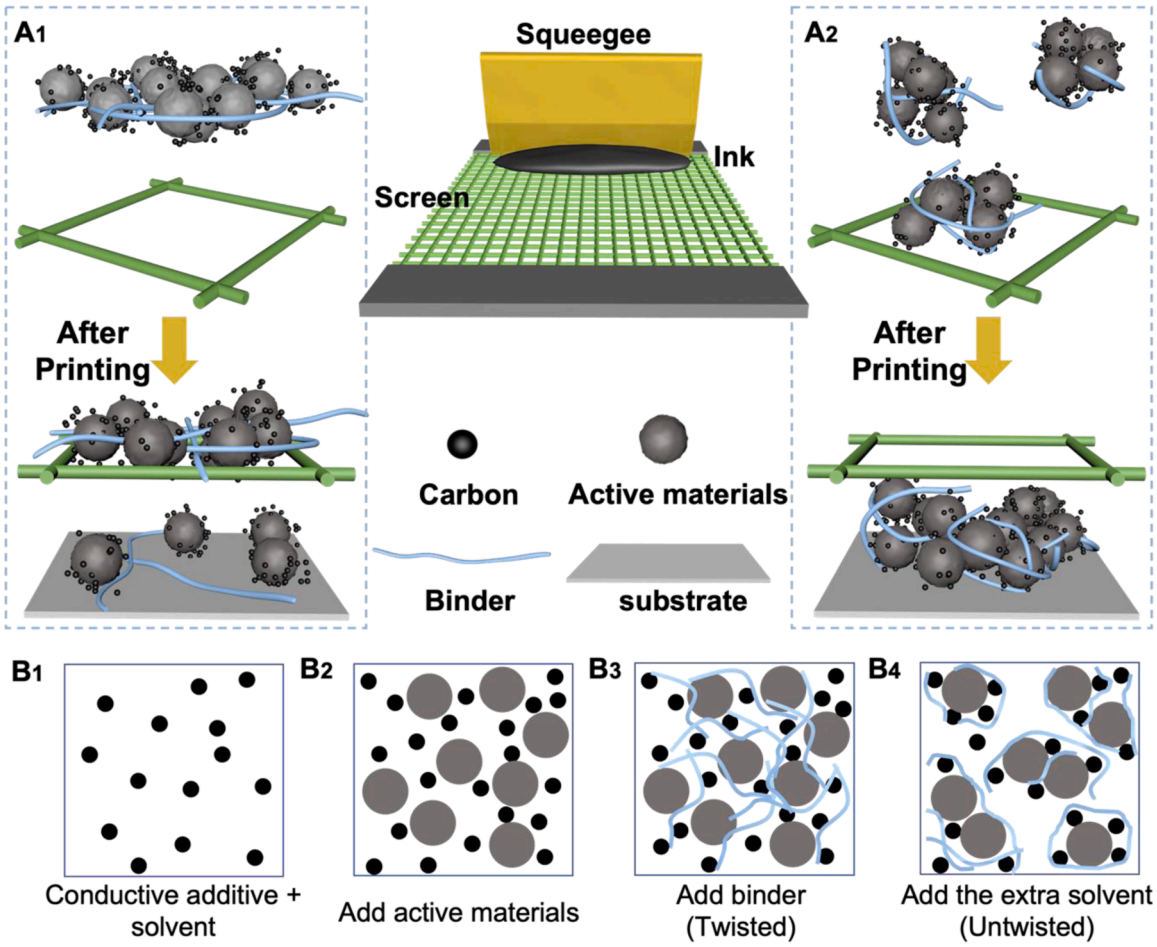

Fig. 1. Schematic of the effects of (A1) twisted and (A2) untwisted molecular chains in the binder on the screen printability of ink. (B1–B4) Schematic of the micromorphological ink structure during the two-step approach ink preparation process.

chains are less twisted than M1 ink. The thixotropy recovery rate and recovery time are the other critical rheological properties for screen-printable inks. Ideally, an excellent screen-printable ink has an almost instant thixotropic recovery rate, which allows the ink to pass seamlessly through the mesh. To mimic and investigate the rheological behavior of inks during a high-speed screen printing process, the thixotropy recovery rates and times were evaluated by a three-step thixotropy test via the successive application of 0.1 s^{-1}, 200 s^{-1}, and 0.1 s^{-1} shear rates in three intervals, 0-90 s, 90-100 s, and 100-200 s. As exhibited in Fig. 2(C), the M1, M2, and M3 inks were 100% recovered at 58, 85, and 36 seconds after being subjected to a high shear rate of 200 s^{-1}, respectively. The shortest recovery time for the M3 ink suggests that this ink can pass through the mesh more facilely than the others, which agrees with the above description.

The screen printability of ink is evaluated by assessing the quality of the printed product. The M1 electrode (Fig. 2(D)) exhibits extensive exposure of the aluminum (Al) foil without transferred particles, demonstrating a low printing quality and poor ink screen printability. Compared to the M1 electrode, the M2 electrode (Fig. 2(E)) shows slightly smaller but still noticeable bare Al foil exposure in the electrode cover region. The improvement in screen printability results from the lower viscosity of the M2 ink than that of M1 ink. In addition, both the M1 and M2 electrodes exhibited no improvement in printing quality during the drying process. The poor printing quality of these electrodes illustrates that T-Inks are not suitable for use in high-resolution printing patterns. In contrast, as presented in Fig. 2(F), there are no visible defects on the M3 electrode printed with the U-Ink; thus, M3 enables precise printing of pattern-integrated electrodes.

Although the reduced solid content can obviously decrease the viscosity and improve the screen printability of inks, the improvement is negligible since the molecular chains within low-solid-content inks remain twisted. To demonstrate this relationship, we evaluated the rheological properties and screen printability of M1 inks under six different solid contents from 50% to 65% (Figs. S2, S3) and that of M2 inks under solid contents from 50%, 55%, and 60% (Figs. S4, S5). Although the viscosity of the ink sharply decreases as the solid content decreases, the screen printability has not been enhanced, obviously. Notedly, observing the shear rate of 200 s^{-1}, the viscosity of the 50% solid content M1 ink (0.49 Pa·s) is lower than the 60% solid content M3 ink (0.65 Pa·s), but the screen printability of M1 ink is still poor. These results demonstrate the screen printability of inks is greatly dominated by the molecular chain status within inks.

To further demonstrate the relationship between the molecular chain status within inks and their screen printability, we designed, prepared, and characterized more T-Inks and U-Inks. The mixing processes of these 60% solid content inks are detailly summarized in Table S1. Briefly, regardless of the initial mixing steps, adding the binder solution in the last step causes the molecular chains inside the produced ink to twist, and introducing extra solvent can open the twisted molecular chains. The corresponding rheological properties are displayed in Fig. S6. The viscosity of T-Inks is marginally higher than that of U-Inks, while the yield shear stress of the former is slightly lower than that of the latter. The viscosity and yield stress differences between the various inks are due to the faint pulling force from the twisted chain networks. Although all T-Inks have a viscosity in the screen-printable region of 1–10 Pa·s and exhibit remarkably quick thixotropic recovery after being subjected to a

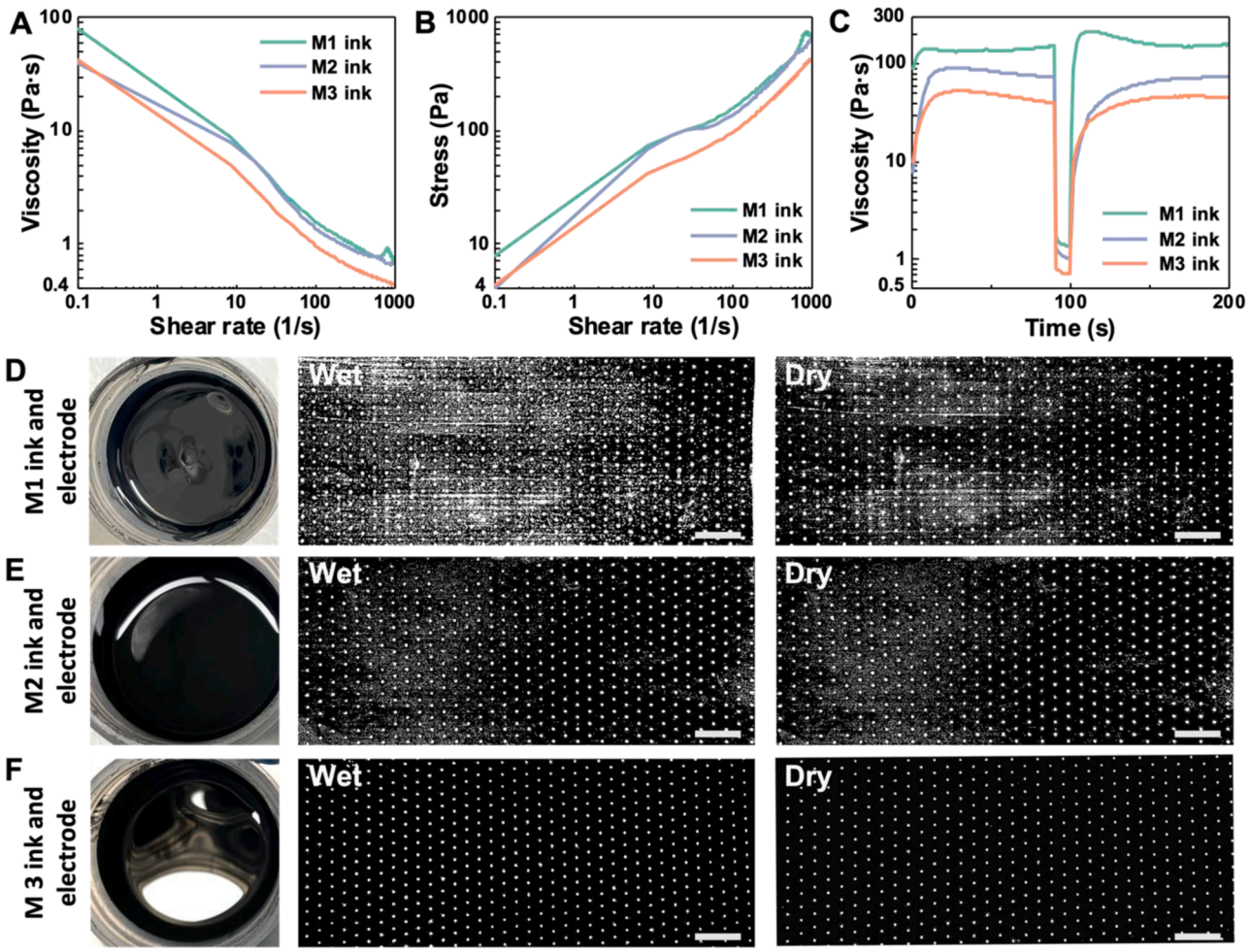

Fig. 2. Rheological properties of the three kinds of prepared inks. (A) Viscosity as a function of shear rate, (B) shear stress as a function of shear rate, and (C) three-step thixotropy test. Optical images of the (D) M1, (E) M2, and (F) M3 inks along with one-layer printed patterns before and after drying; the scale bars are 4 mm in length.

high shear rate, their screen printability is still poor. Although these eight inks are evenly mixed from a macro perspective, the printing quality of electrodes screen-printed using these inks differs. As demonstrated in Fig. S7, conspicuous defects are only apparent in the electrodes screen-printed using T-Inks, while the quality of the electrodes printed using U-Inks is outstanding.

The morphology of the M1, M2, and M3 electrode coating areas was further characterized using scanning electron microscopy (SEM) to evaluate the printing quality and component dispersion in more detail. Top-view images were collected for the one-layer printed electrodes on bare Al foil, and cross-sectional images were taken for the multilayer printed electrodes. The low-magnification SEM images depict the screen printability and conductive additive distribution of the printed electrodes. Consistent with the previous discussion, the M1 and M2 electrodes exhibit poor screen printing quality. Two large bare Al foil regions with a small amount of scattered adhered active material are visible on the M1 electrode (Fig. 3(A1)), and many unexpected holes are visible on the surface of the M2 electrode (Fig. 3(B1) and highlighted in Fig. S8(A)). In comparison, Fig. 3(C1) displays the surface of the printed M3 electrode is flat and smooth without apparent defects. The printing quality affects the electrochemical properties of as-printed electrodes by influencing their internal structure. In addition to the printing quality, the dispersion of the components, especially the uniformity of the dispersion of carbon particles, determines the electrochemical performance of Li-ion batteries. Homogeneously dispersed carbon particles create interlinking channels, improve electron transfer in the cathode electrode, and ensure outstanding rate performance. As presented in Figs. 3(A1) and 3(C1), the high-quality printed regions of the M1 and M3 electrodes present a uniform carbon particle distribution. In contrast, some carbon particle aggregates appear on the surface of the M2 electrode. Thus, compared to the M1 and M3 inks, the carbon particle distribution of the M2 ink is unsatisfactory. The images at 10 × magnification expand the features of each electrode. Excitingly, net-like structures generated by the twisted molecular chains are hidden inside a well-printed region within the M1 electrode, as shown and highlighted in Figs. 3(A2) and S8(B). The length of one observable chain is approximately 20 μm, nearly half the distance between two fibers in our screen mesh (48 μm). Therefore, large amounts of net-like structures can work as additional nets and pull on the particles so that they remain on the surface of the screen. Fig. 3(B2) displays a tiny defect region in Fig. 3 (B1), in which many carbon particles are aggregated without the inclusion of NMC 622 particles. Unlike the M1 and M2 electrodes, no net-like structure is observed, and the carbon particles uniformly encapsulate NMC 622 particles on the M3 electrode, as shown in Fig. 3(C2).

Cross-sectional SEM images of multilayer-printed M1, M2, and M3 electrodes are displayed in Figs. 3(A3), (B3), and (C3). The multilayer printing process maintained an electrode mass loading of approximately 6.5 mg/cm^2 and a thickness of approximately 38 μm on a rugged substrate. Different from the M2 and M3 electrodes, the M1 electrode is distinctly uneven, with some discontinuous contact between particles. Therefore, even though printing more layers can increase the mass loading of electrodes, their internal structural drawbacks cannot be

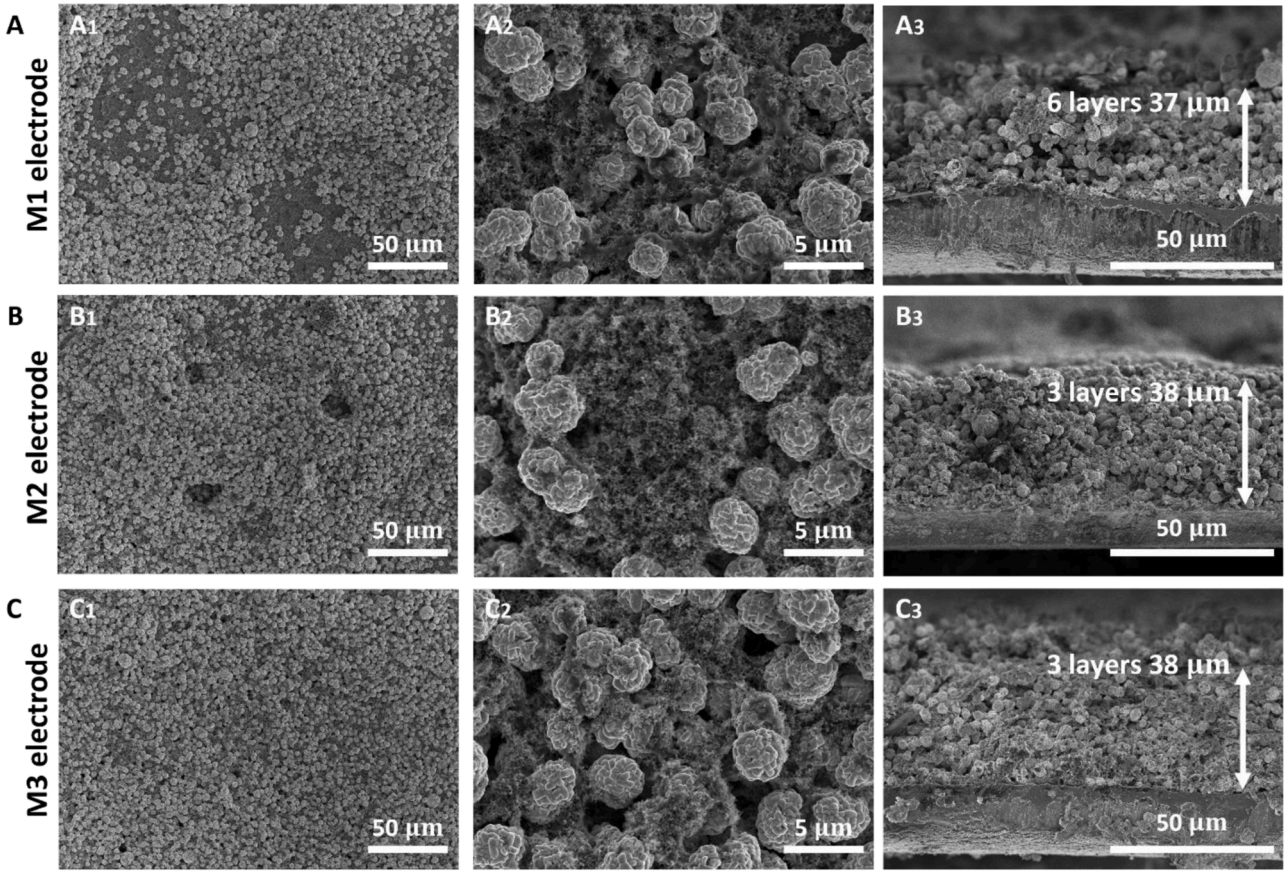

Fig. 3. SEM images of printed electrodes. Top-view low-magnification images of one-layer printed (A1) M1, (B1) M2, and (C1) M3 electrodes. Top-view high-magnification images of one-layer printed (A2) M1, (B2) M2, and (C2) M3 electrodes. Cross-sectional images of (A3) M1, (B3) M2, and (C3) M3 electrodes.

fixed entirely. More importantly, the M1 electrode was printed with six layers to achieve the target mass loading, while the M2 and M3 electrodes were printed with three layers. Obviously, the more layers required for printing, the higher the cost of the industrial manufacturing process. Therefore, poor screen printability destroys the accuracy and reduces the manufacturing efficiency of printed electrodes for achieving the same mass loading.

For a more comprehensive analysis of the relationship between inks and the component distribution within screen-printed electrodes, XCT was employed to study and label the distributions of NMC 622 (yellow), super P (red), PVDF (green), and pores (blue) for screen-printed one-layer M1, M2, and M3 electrodes. All computed tomography areas were materials-printed area and the larger blue areas indicate the worse printability. In contrast to SEM, which only evaluates the local surface morphology, XCT is a powerful approach to segmentally scan, probe the internal structure, and generate 3D reconstructions of screen-printed electrodes [29]. A 2D image of the M1 electrode is shown in Fig. 4(A), in which the blue color corresponds to pores. A large number of blue areas demonstrate the relatively poor printing quality of the M1 electrode. The distribution of NMC 622 is highlighted in Fig. 4(B) in yellow. As the matrix material, NMC 622 particles are densely located on the well-printed area but are more sparsely located at apparent edges of defects. In Fig. 4(C), super P is labeled in red. In addition to being greatly hindered by unexpected defects, the dispersion of super P is unsatisfactory within defect-free areas. Even worse, a large amount of binder is aggregated inside the M1 electrode, as marked in green in Fig. 4(D). Therefore, the twisted molecular chains within the M1 ink not only impair its screen printability but also negatively affect the dispersion of the binder in the screen-printed electrode. Despite having slightly smaller hole areas than the M1 electrode, the M2 electrode is still displayed to be incomplete (Fig. 4(E)). Furthermore, carbon and binder are highly aggregated in the M2 electrode. Compared to the M1 electrode, the carbon even shows a high degree of aggregation in the electrode (Fig. 4(G)). Meanwhile, a large amount of green parts in Fig. 4(H) clearly shows that the distribution of the binder is also uneven in the M2 electrode. And the larger amount of green parts within the one-layer printed M2 electrode results from the more electrode-covered area than that of the one-layer printed M1 electrode. The 2D image of the M3 electrode is exhibited in Fig. 4(J), in which the blue areas refer to pore areas, and the M3 electrode has far fewer pores than the M1 and M2 electrodes. Moreover, NMC 622 occupies the main fraction of the M3 electrode and forms an integrated area. Compared to the component dispersion within the M1 and M2 electrodes, the M3 electrode has a more homogeneous and reasonable distribution of carbon (Fig. 4(L)) and the binder (Fig. 4(M)). In short, inks with untwisted molecular chains can ensure high printing quality and uniform distribution of constituent materials. In addition to the carbon distribution being important, structural integrity is essential to Li-ion batteries. Twisted molecular chains generate many unexpected voids that damage the interconnections within screen-printed electrodes and further compromise their electrochemical performance. Predictably, this situation can be worsened after multiple screen printings.

To evaluate the effects of the structural integrity and component dispersion within printed electrodes on their electrochemical properties, screen-printed M1, M2, and M3 electrodes were assembled in coin cells with Li metal as the anode. The cyclic voltammetry (CV) curves (Fig. 5 (A)) show clear oxidation peaks at approximately 3.9 V and reduction peaks at approximately 3.6 V for all electrodes, corresponding to the redox transition of Ni^{2+}/Ni^{4+} [30]. The peak separation implies an overpotential. The potential gap of the M3 (247 mV) and M2 (250 mV)

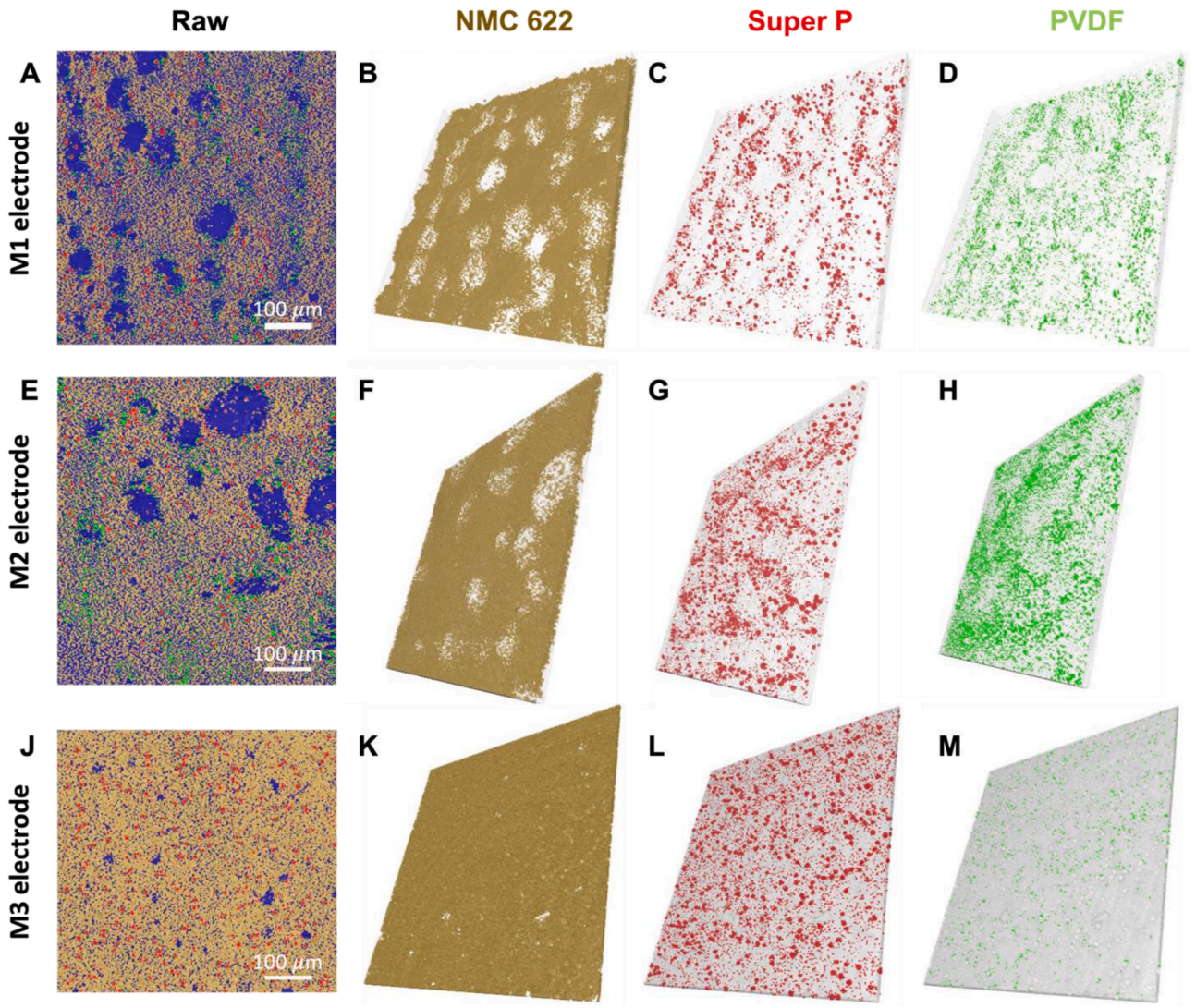

Fig. 4. Distributions of NMC 622, super P, and PVDF in one-layer printed M1 and M3 electrodes were revealed by XCT. Reconstructed 2D images of the screen-printed (A) M1, (E) M2, and (J) M3 electrodes. 3D segmented images of the (B-D) M1 electrode, (F-H) M2 electrode, and (K-M) M3 electrode with the element distributions.

electrodes are much smaller than that of the M1 (352 mV) electrode, indicating that the M3 and M2 electrodes have better reaction kinetics and a lower degree of polarization than the M1 electrode. The large overpotential in the M1 electrode mainly results from poor structural integrity and weak interconnection between components within the printed electrodes.

The first three charge and discharge curves of the M3 electrode at a current rate of 0.1 C are displayed in Fig. 5(B). The initial charge and discharge capacities of the M3 electrode are 201 and 173 mAh/g, respectively. The initial Coulombic efficiency is 86.1%, and the first cycle inefficiency mainly results from the formation of a solid electrolyte interface (SEI) on the electrode. The following two cycles exhibit similar charge and discharge capacities, suggesting that screen-printed M3 electrodes are reasonably stable. The Nyquist plots of the M1, M2, and M3 electrodes are compared in Fig. 5(C). All batteries exhibit semicircles in the high-frequency region and Warburg tails in the low-frequency region; these features indicate the charge transfer resistance and ion diffusion resistance, respectively. The charge transfer resistance of the M1, M2, and M3 electrodes sequentially decreases, which reflects the effect of the ink preparation process on the charge transfer kinetics. The low charge transfer resistance of the M3 electrode is attributed to the uniform carbon distribution and complete and continuous internal electrode architecture.

The rate performance of these screen-printed electrodes was evaluated by changing at various rates of 0.1, 0.5, 1, 2, 4, and 6 C, and constant discharging at C/3, as exhibited in Fig. 5(D). At 0.5 C, the M3 electrode (175 mAh/g) exhibits a superior charge capacity than the M1 (163 mAh/g) and M2 (163 mAh/g) electrodes, and the advantage is even more apparent at high rates. At 6 C, the charge capacity of the M3 electrode is 141 mAh/g, which is much higher than those of the M1 (106 mAh/g) and M2 (110 mAh/g) electrodes. This result agrees that the M3 electrode has a lower charge transfer resistance. The substantial specific capacity of the M3 electrode at a high current rate is attributed to the more complete and continuous internal architecture and more uniform binder dispersion than the M1 electrode, as well as the more uniform carbon distribution than the M2 electrode. The long-term cycling performance of the screen-printed M1, M2, and M3 electrodes at a charge rate of 1 C and a discharge rate of C/3 is shown in Fig. 5(E). All cells were initially activated at 0.1 C and 0.5 C for three cycles. When cycled at 1 C, the M3 electrode exhibited a specific charge capacity of 171 mAh/g. Concurrently, the electrode maintained superior capacity retention of 81.0% and high Coulombic efficiency of 98% for 100 cycles. Noteworthy, the M1 electrode exhibits significant charge capacity that decays at approximately 65 cycles. Moreover, the Coulombic efficiency of

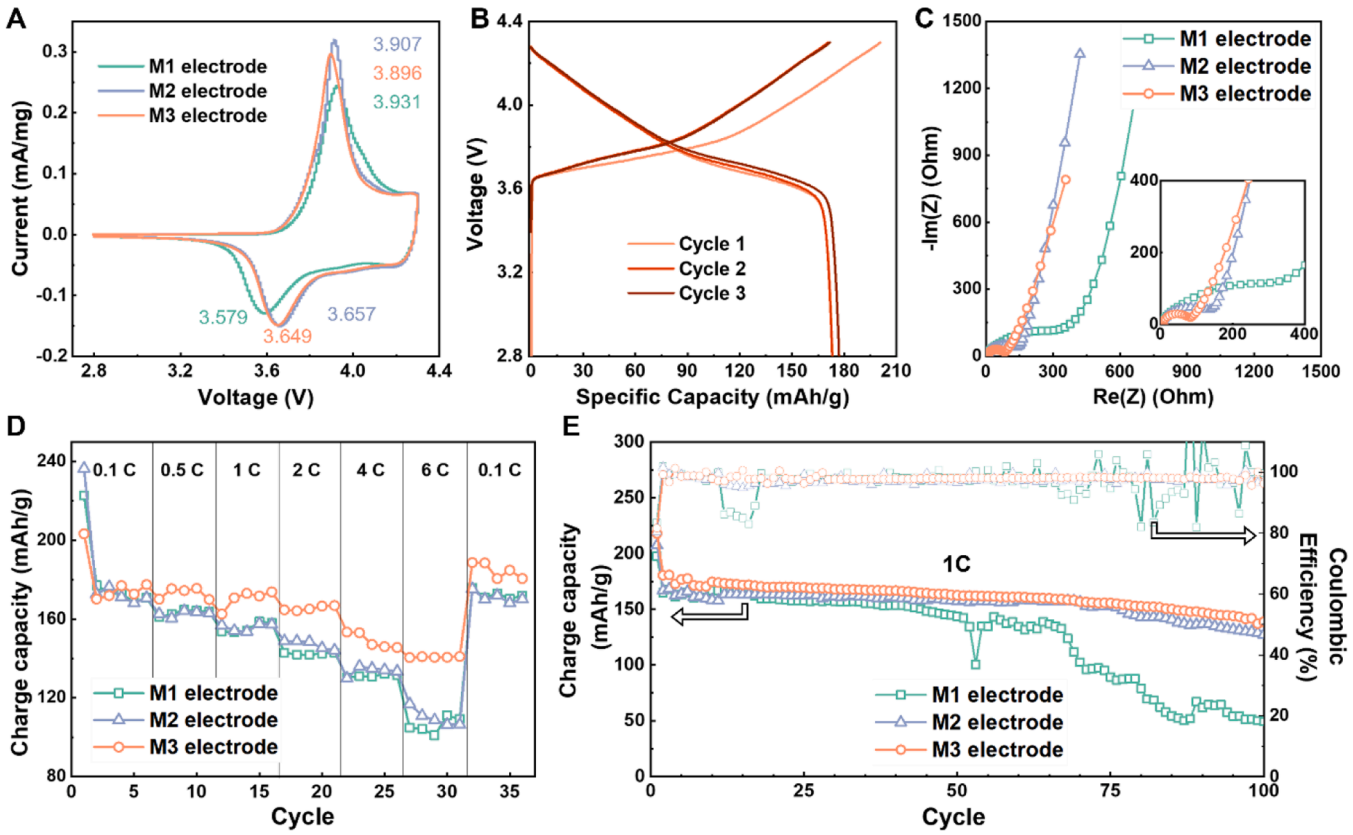

Fig. 5. Electrochemical performance of screen-printed electrodes. (A) CV curves of the as-printed electrodes. (B) Galvanostatic charge and discharge curves of the M3 electrode at 0.1 C. (C) Nyquist plots, (D) rate performance, and (E) long-term cycling performance of screen-printed M1, M2, and M3 electrodes.

the M1 electrode is unstable and vigorously fluctuates starting from 70 cycles. Both the unsatisfactory charge capacity stability and fluctuating Coulombic efficiency of the M1 electrode are ascribed to its lack of architectural integrity. The long-term cycling performance of three kinds of electrodes at a high charge rate of 6C and a discharge rate of C/3 is exhibited in Fig. S9. At a high current rate, the stability of all the cells has been significantly reduced due to the lithium metal dendrite issue. In the initial 20 cycles, the M2 electrode displayed the lowest charge capacity due to its carbon dispersion is nonuniform. The M1 electrode exhibits dramatic decay of charge capacity from 35 cycles because of its nonuniform components interconnection with the twisted binder. Therefore, a complete and continuous internal architecture and a homogeneous component distribution are critical for printed electrodes to achieve superior electrochemical performance.

Understanding the mechanism and optimizing preparation parameters are crucial for the scale-up of the novel ink preparation process, i.e., the two-step approach, for large-scale screen-printed electrode manufacturing. The stepwise addition of NMP has different functions with respect to the properties of inks: the first NMP addition disperses carbon with a high specific surface area, and the second NMP addition can open twisted molecular chains and improve the screen printability of the ink. Therefore, the proportions of NMP added in the first and second steps during untwisted ink fabrication (named "1st sol-2nd sol") influence the micromorphological structure of the ink. To investigate in detail the effect of the 1st sol-2nd sol value on inks prepared by the two-step approach, 60% solid content M3 inks were prepared with 1st sol-2nd sol values of 75%-25% (75% of NMP is mixed in the first step, and the other 25% is mixed in the second step; other labels follow a similar nomenclature), 80%-20%, 85%-15%, and 90%-10%.

The rheological properties and screen printability of the above-mentioned inks were measured. The viscosity of these inks increases with the 1st sol-2nd sol value, as shown in Fig. 6(A). At a shear rate of 0.1 s^{-1}, the viscosity of the 90%-10% ink (45.5 Pa·s) is over six times that of the 75%-25% ink (6.9 Pa·s). The viscosity of the low 1st sol-2nd sol inks (where more NMP is mixed in the second step than in the first step) indicates their components have weak connections. Fig. 6(B) shows the 100% recoverability of these inks in 60 s after supporting a high shear rate of 200 s^{-1}. Results indicate the rheological properties of these inks are in a reasonable screen printable region. To further evaluate the printability of these inks under different conditions, screen printing was performed on a bare Al substrate using a 300 mesh screen with pores 0.5 mm in diameter and a 420 mesh screen with pores 0.3 mm in diameter, as described in Fig. S10. Benefiting from the untwisted molecular chains, all inks display outstanding printability with the 300 mesh screen. However, M3 inks with various 1st sol-2nd sol values exhibit greater differences in screen printability for the high (420)-mesh screen, and the quality of as-printed electrodes weakens with increasing 1st sol-2nd sol value.

As mentioned above, the composition distribution and the internal structural integrity of the electrode significantly affect the electrochemical performance of screen-printed electrodes, and these factors are affected by the 1st sol-2nd sol value during ink preparation in the two-step approach. For example, ink with a high 1st sol-2nd sol value (where more NMP is mixed in the first step than in the second step) has a homogeneous carbon distribution because a large amount of solvent is added in the first step; however, the internal structural integrity of the resulting as-screen-printed electrode will be lacking owing to the limited screen printability. Therefore, adjusting the 1st sol-2nd sol value is an effective pathway to fabricate the best screen-printed electrode in different situations to balance the carbon distribution and internal structure and further achieve outstanding electrochemical properties. The rate performances of M3 electrodes with different 1st sol-2nd sol values are displayed in Fig. 6(C), wherein the half-cell was charged at 0.1, 0.5, 1, 2, 4, and 6 C and discharged at C/3. All screen-printed

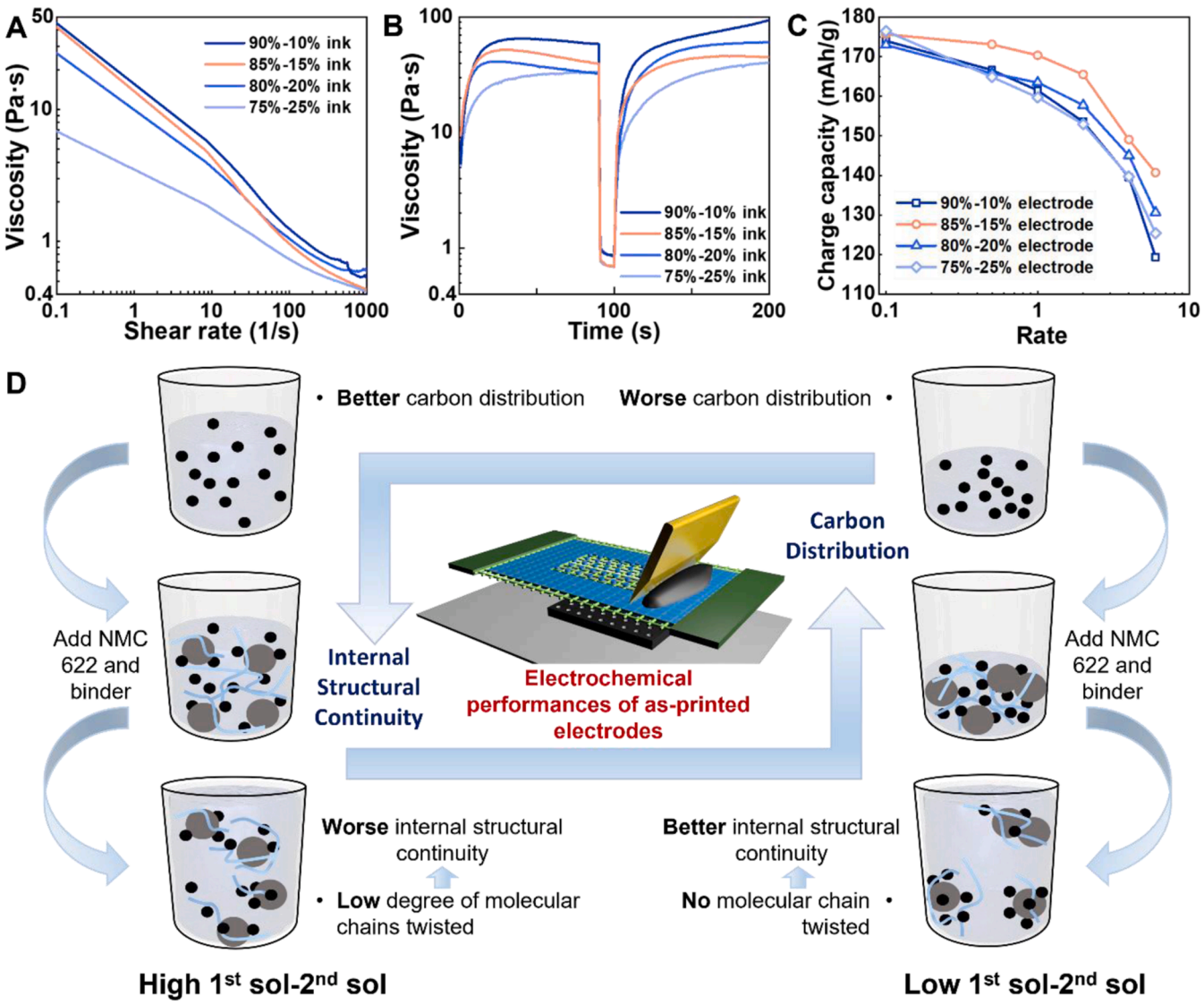

Fig. 6. Development of the proposed ink preparation process. Rheological properties of M3 inks prepared with various 1st sol-2nd sol values: (A) viscosity as a function of shear rate and (B) three-step thixotropy test (0.1, 200, and 0.1 s^{-1} shear rates were applied in three intervals, 0-90 s, 90-100 s, and 100-200 s). (C) Rate performance of M3 electrodes fabricated with different solvent addition ratios. (D) Schematic of the effect of the solvent addition ratio on the material distribution during mixing of inks with the same solid content fabricated by the two-step approach.

electrodes exhibit excellent and similar specific charge capacities at the low test rate of 0.1 C (174, 176, 173, and 175 mAh/g for 90%-10%, 85%-15%, 80%-20%, and 75%-25% electrodes, respectively). Starting from 0.5 C, the 85%-15% electrode displays a higher specific charge capacity (173 mAh/g) than the other electrodes (~166 mAh/g), and the difference increases with the increasing current rate. At 6 C, the 85%-15% electrode exhibits a specific charge capacity of 141 mAh/g, which is higher than those of the 90%-10% (119 mAh/g), 80%-20% (131 mAh/g), and 75%-25% (125 mAh/g) electrodes.

The underlying mechanism of the effects of the 1st sol-2nd sol value on the carbon distribution and screen printability of inks fabricated by the two-step approach is illustrated in Fig. 6(D). With a low 1st sol-2nd sol value, a lower amount of solvent in the first step impacts the homogeneity of the carbon particle dispersion. This inhomogeneity is further exacerbated by adding NMC 622 particles and a highly viscous binder solution. Concurrently, the subsequent addition of more solvent is helpful for opening twisted molecular chains while enlarging the distance between the well-dispersed units. A large distance between these well-dispersed units can weaken their mutual forces and decrease the viscosity of the ink, thus reducing the difficulty of transporting the well-dispersed units through the mesh and achieving well-printed patterns and an electrode with a complete integral structure.

To better understand the underlying mechanisms by which different methods affect the ink printing quality, we developed a CGMD model to both qualitatively describe the effects of the shear flow behavior in the printing process and quantitatively characterize the viscosities under different shear rates (Fig. 7), based on our previous studies [31,32]. NMC 622 particles (Figs. S11 and S12(A)) were modeled as spherical particles with a diameter of 3.5 μm. The binder (Fig. S12(B)) was modeled as coarse-grained polymer chains. Super P particle (Fig. S12(C)) was modeled as a series of point-like spherical particles. The solvent was implicitly considered by using its density and viscosity as inputs through the lattice Boltzmann method (LBM). Based on the measured component distributions and the fixed addition pathway in the experimental preparation procedures (Fig. S13(A-C)), the three preparation methods are illustrated using one-to-one correspondence CGMD simulation. The configuration for the final addition path was adopted to perform a simulation for a sufficiently long time using LBM integration to obtain the equilibrium configuration. The obtained equilibrium configurations for the three preparation methods are shown in Fig. 7

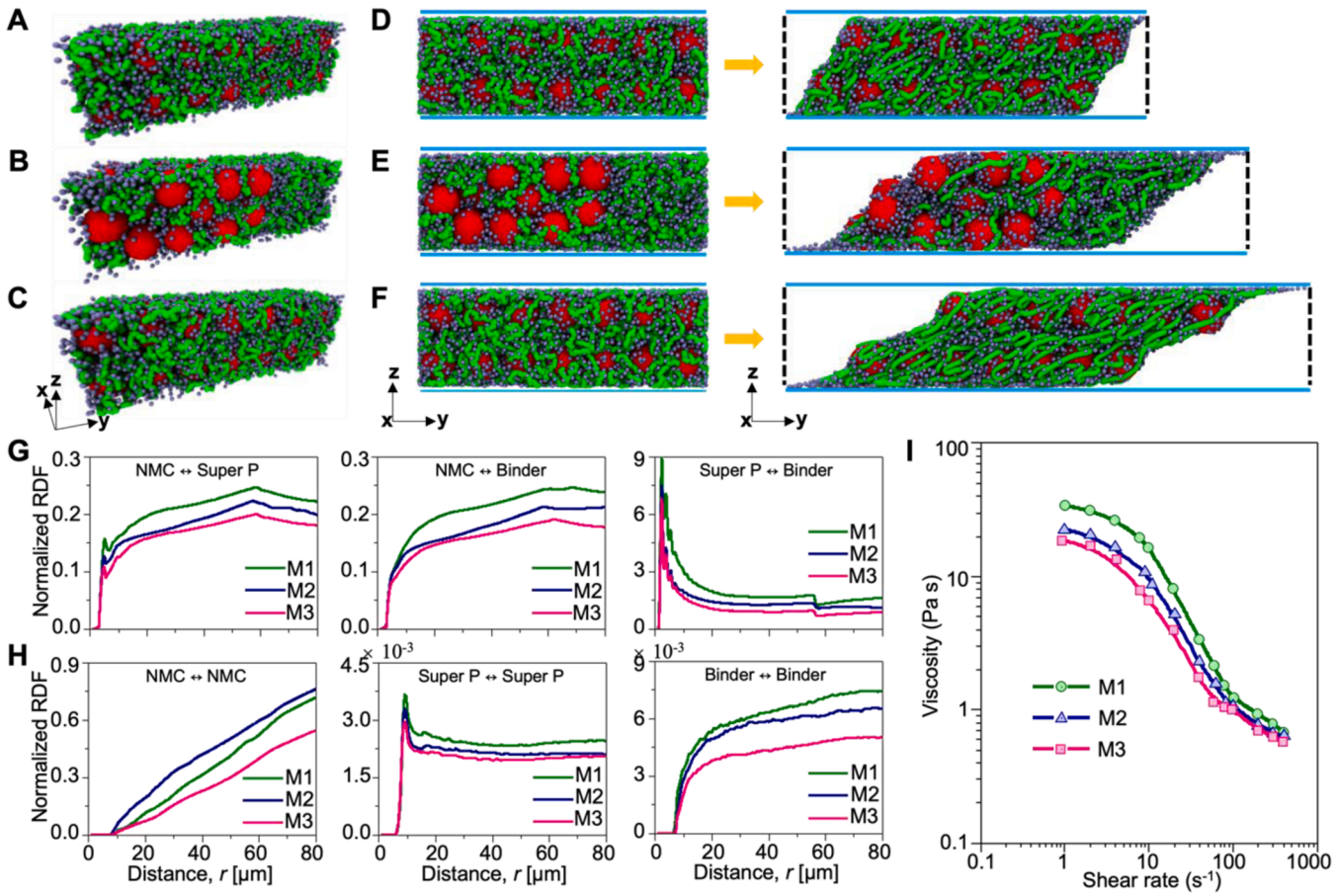

Fig. 7. Equilibrium configurations for the (A) M1, (B) M2, and (C) M3 systems. Snapshots of the shear behavior at a shear rate of 20 s^{-1} for the (D) M1, (E) M2, and (F) M3 systems with increasing simulation time from 0 (left) to 0.553 s (right). Radial distribution functions (RDFs) after shear application for (G) the different types of particles and (H) the same types of particles for the three methods. (I) The viscosity of inks prepared by the three methods as a function of shear rate.

(A–C).

Based on the equilibrium configurations, we first conducted shear flow simulations to qualitatively describe the effect of the different methods on the shear behavior of the ink during the printing process. Periodic boundary conditions were applied in the x and y directions, while the z direction was bounded by two flat plates. A shear velocity of 20 s^{-1} was applied on the top flat plate corresponding to the z-plane to drive the shear flow. Fig. 7(D–F) shows snapshots of the ink printing processes of the three methods at two times with different states: 0 s (left) before a shear flow is applied; 0.553 s (right) after the shear flow is applied to the top plate. Under the same shear flow and timescale, particle aggregates tend to expand most easily in the M3 system, followed by the M2 and M1 systems. In addition, the compactness or fluidity of particles was quantified by the interparticle radial distribution function (RDF). Fig. 7(G) and (H) show the RDFs for different types and the same types of particles, respectively. Except for the inter-NMC particle RDFs, the RDF amplitudes for the particles show an increasing trend in the order M3, M2, and M1, which indicates that M3 can lead to the best shear fluidity. The inter-NMC particle RDF amplitude is the highest in the M2 system, which is caused by the local concentration of more NMC particles in the initial configuration and the limited timescale of the shear flow. To illustrate this point, we have plotted the inter-NMC particle RDFs for the initial configurations (0 s) in Fig. S14. The comparison shows that the inter-NMC particle RDF amplitude is the highest in the M2 system. However, the decrease rate of the RDF amplitude in the M2 system is higher than that in the M1 system and close to that in the M3 system. That is, if the timescale is long enough, then the inter-NMC particle RDF amplitude in the M2 system will be between those in the M1 and M3 systems. The RDF amplitudes for all the particles are lowest in the M3 system because the system moves further within the same timescale, leading to increased particle spacing and a more dispersed distribution between particles. Conversely, the M1 system spreads outward only slightly within the same timescale, which gives rise to poor mass transport for particles and denser particle distribution. Similarly, the RDF amplitudes for all the other particles in the M2 system are between those in the M1 and M3 systems because the diffusion velocity of the M2 system is between those of the M1 and M3 systems within the same period, leading to a middle range of particle dispersion. These qualitative findings and the fluidities of the inks considered suggest that M3 can lead to a better quality of ink for printing, followed by M2 and M1.

In addition, we directly calculated the viscosity under different shear rates to quantitatively characterize the effects of different methods on the quality of the printing ink. The traditional method of calculating the viscosity, which only applies a flow velocity at the top plane to emerge the velocity gradient between the top and bottom plane. Generally, the expression can be described as where is the viscosity, the thickness normal to the velocity direction, the cross-sectional area, the flow velocity applied at the top, and the force on the top. However, with this traditional method, extracting the force on the top is currently difficult to compute. Here, an alternative, experimentally verified approach (Fig. S15) was used to calculate the viscosity of ink in a rectangular channel [33]. The viscosity is expressed as where is the viscosity, the shear stress, and the shear rate. The simulation setup for the alternative approach can be found in Fig. S9(D). According to the alternative approach, Fig. 7(I) shows the viscosity of the inks prepared by the three

methods as a function of shear rate. The viscosity is lowest for the M3 ink, followed by the M2 and M1 inks. Generally, viscosity describes the resistance of a fluid to a change in deformation or to the movement of contiguous portions relative to one another; this parameter can also be described as opposition to flow. Therefore, a lower viscosity indicates that less force or energy is required to make a fluid flow. Likewise, forced liquid flow can be easily achieved in lower-viscosity systems by applying the same force or energy. Under the same shear force, the M3 system can easily overcome the resistance during the ink printing process, and particles spread easily due to its lowest viscosity, leading to good printing quality. However, for the M1 system with the highest viscosity, the same shear force is insufficient to overcome the intrinsic deformation resistance and force liquid flow, which makes particle diffusion difficult and leads to worse printing quality. Similarly, the viscosity of the M2 system lies between those of the M1 and M3 systems, and the ability of the applied shear force to induce fluid flow is also in the middle. In addition, from a modeling point of view, the relaxation of the system and the physical force imposed in the last step in M3 can effectively enhance particle dispersion, which can maintain particle flow at faster speeds and lead to a lower viscosity. These findings indicate that M3 can lead to the best quality screen printing ink, followed by M2 and M1.

3. Conclusion

In this work, for the first time, we opened the twisted molecular chains of the binder in the printing ink to achieve both excellent printability and improved battery performance. Considering that the internal architectural continuity and component distribution of printed electrodes determine their electrochemical performance, we developed an innovative scalable ink preparation process—a two-step approach of dropwise adding solvent to open the twisted molecular chains and ensure the distribution of components within inks. We prepared a screen-printable $LiNi_{0.6}Mn_{0.2}Co_{0.2}O_2$ cathode ink with ultrahigh (60%) solid content using the two-step approach. The screen-printed electrode exhibits a higher charge capacity of 141 mAh/g at 6 C than the electrode with a suboptimal carbon distribution (110 mAh/g) and the electrode with weak continuity of internal electrode structure and inhomogeneous binder distribution (106 mAh/g). Moreover, the screen-printed electrode fabricated by the two-step approach has adequate stability at 1 C (capacity retention of 81.0 % after 100 cycles), which is much better than the one with poor screen printing quality by utilizing the molecular heavily twisted ink. The results emphasize the relationship between printing quality, internal architecture, and the cycling stability of electrodes. Additionally, we revealed the mechanism of the two-step approach: the first part of the solvent disperses the components and the second part of the solvent opens the twisted molecular chains. Based on it, we studied the pathways to optimize the ink to fabricate composition homogeneity and internal structure continuity of screen-printed electrodes in various situations. Furthermore, we employed coarse-grained molecular dynamics to study the component distribution within inks and the shear behavior of inks during the printing process, and their fluidity was explored using the lattice Boltzmann method. The proposed straightforward and low-cost ink preparation strategy can be scaled up to manufacture large-scale R2R screen printing and can potentially facilitate research and industrial manufacturing on architecture design for screen-printed electrodes.

4. Experimental section

4.1. Materials

The prepared high solid content inks consist of Muticristalline NMC 622 (diameter of 3.5 μm from Nanoramic Laboratories), Super P (diameter in 40 nm from MTI Corporation), homopolymer PVDF (Kureha 7200 with an average molecular weight of $6.3*10^5$ g mol^{-1} and inherent viscosity in 2.1 dl/g purchased from Kureha Company), and NMP (Fisher Science Education) as active material, a conductive additive, binder, and solution, separately. NMC 622 particle size distribution is shown in Fig. S11. Before the utilization, NMC 622 and Super P were dried under a vacuum oven for at least 12 h, and the PVDF was dissolved into NMP to get a concentration of 10 wt.%. All chemicals and materials were utilized without additional processing.

4.2. Ink preparation

The above materials were mixed following the steps shown in Fig. S1 and Table S1. All inks were prepared as NMC 622: Super P: PVDF = 94:4:2 in the formulation and 5 g for total weight per batch. Herein, Method 3 is highlighted because of its excellent printability and battery performance of printed electrodes. First, 0.12 g Super P and the first part of NMP were mixed in a plastic cup (20 mm in diameter); following it, 2.82 g NMC 622 was added and mixed; and then, 0.6 g dissolved at 10 wt.% PVDF were added and mixed; finally, the second part of NMP was added and then mixed the whole materials to homogeneous. NMP added a total of 1.46 g. The mixing processes were done by a dual asymmetric centrifugal mechanism (DAC 330-100 Pro Speedmixer from FlakTek). For each mixing process, materials withstood 1500 rpm for 30 seconds, 2500 for 30 seconds, and 3500 rpm for 240 seconds. The variables were controlled by preparing all the inks with the same total mixing time. Although the total NMP was kept, The ratio of NMP added in the first and the second steps were controlled and labeled as 75%-25%, 80%-20%, 85%-15%, and 90%-10%.

4.3. Screen printing

The pattern for electrode printing was designed using Adobe Illustrator software (Adobe Inc.), and the pattern dimensions of 4.5 cm 12 cm with circles of 0.5 cm in diameter. The 300 mesh screen were purchased in the market, and the thickness of the total screen and emulsion is around 60 μm for electrode printing. Due to the differences in printability for various inks, adjusting the printing layers has been done to keep the same mass loading (around 6.5 mg/cm^2) of printed electrodes for the electrochemical properties evaluations. Specifically, three layers of printing work for electrodes printed with M2 and M3 inks, and six layers of printing works for that with M1 ink. The theoretical density of the as-prepared electrode is 2.66 g/cm^3, which is calculated by $\rho_{mix} = \sum \rho_i * Xi$, where Xi is the volume fraction of each component. The porosity of M1, M2, and M3 electrodes are 34.8 %, 36.5 %, and 37.2 %, respectively. And the channels distribute as follows: 0.5 mm in channel diameter and 2 mm in edge distance of channels. The double sides carbon-coated Al foil (Suzhou Sineno Technology Co., LTD) is used as both the current collector and substrate to evaluate the electrochemical properties of screen-printed electrodes. However, the black carbon-coated layer makes it difficult to distinguish the printability of inks. An Al foil (MTI Corporation) is used as the substrate to display the printability of inks.

4.4. Characterization methods

The morphology of the samples was observed by Hitachi S4800 SEM at 3 kV. The rheological properties were measured by a discovery hybrid rheometer (Discovery HR-30) from TA-Instruments with a flat Peltier plate.

4.5. X-ray computed tomography

The XCT measurement was carried out using a Zeiss Xradia Versa 520 XCT unit. The data were obtained over a sample rotation of $\omega = 360^\circ$ with 1601 projections at equal steps. The data were collected using 4 × and 20 × scintillator objectives for two separate magnifications. The 4 × scans were collected at 40 kV at 3 W, and 20 × scans were used at 60

kV at 5 W. The higher power was used at 20 × to increase the counts because the scintillator screen was significantly thinner for the 20 × scintillator objective. A 2 × 2 binning was used for optimized resolution and measurement time. The resultant pixel sizes for the 4 × and 20 × scans were 1.03 μm and 0.65 μm, respectively. An ORS Dragonfly PRO v.3.5 software was used for image processing and segmentation.

4.6. Electrochemistry characterization

In all the electrochemical measurements, the electrolyte was 1.2 M $LiPF_6$ dissolved in EC: EMC= 3: 7 by weight (Gen). 80 μL of the electrolyte was added to the cell during the assembly. The Celgard 2400 (25 m in thickness) was used as the separator. The active materials mass loading of screen printed electrode was around 6.5 mg/cm^2. EIS was performed using an electrochemical station (Biologic SP150) in the frequency range of 1 MHz to 100 mHz at room temperature, and cyclic voltammetry (CV) was carried in the range of 2.8 V-4.3 V using Biologic MPG2 in the scan rate of 0.1 mV/s. Galvanostatic tests were performed using a LANDT 8-channel tester (Wuhan LAND Electronic Co., Ltd.). The rate performance was discharged at C/3 and charged at different C-rate, respectively, 0.1 C for six cycles, then 0.5 C, 1 C, 2 C, 4 C, and 6 C for five cycles, respectively, and finally recovered to 0.1 C for another five cycles. All the electrochemical tests were run at room temperature, and active material capacities were reported.

5. Computational model and method

5.1. Model system

To study the influence of three experimental methods on printing ink quality, we qualitatively studied their shear flow behaviors during printing and calculated the viscosity of their equilibrium configurations by using numerical simulations. The three methods simulated by coarse-grained molecular dynamics corresponding to the experiments are described as follows. For method 1 (M1), super P is first evenly distributed in the simulation box. Then, NMC 622 particles are added into the simulation box, keeping both super P and NMC 622 particles distributed evenly in the solvent. After that, binders are placed on the top of the simulation box, making them evenly fill the space left behind. For method 2 (M2), NMC 622 and super P particles are first separately concentrated and then assembled into the simulation box. Next, the binders are added to the top of the simulation box and let them fill the space left behind. For method 3 (M3), super P particles are first evenly distributed in a simulation box accounting for 90% of the volume of the final simulation box (Equivalent to adding 85% solvent). Next, NMC 622 particles are added to the simulation box, keeping both super P and NMC 622 distributed uniformly in the solvent. Then, binders are added to the top of the simulation box, making them evenly fill the space left behind. After that, the simulation box is further relaxed, and an equilibrium simulation is performed by applying a body force to the solvent to let these binders feather off. Ultimately, the equilibrium configurations of the three methods (M1∼M3) are obtained by performing a longtime simulation using the Lattice Boltzmann method (LBM). The simulation box is 10 × 30 × 10 μm^3, in which periodic boundary conditions are applied in the x and y directions, while the z-direction is bounded by two flat plates.

5.2. Fluid model

Lattice Boltzmann method (LBM) is an efficient solver to recover Navier-Stokes equations for fluid flow [34], which has been widely used to solve fluid dynamics at the milliliter scale [35–37]. The density distribution function is the essential quantity of LBM in phase space, which can be employed to determine the density (ρ) and velocity (u) of fluid. Generally. LBM is considered an accurate second-order method in both time and space. The mathematical derivation of LBM, relationships between the two macro variables, ρ, u, and density distribution function, can be found in our previous studies [38]. In this work, a solvent is implicitly considered by using its density and viscosity as inputs. The density and viscosity of NMP solvent are 1.03 g cm^{-3} and 1.89 × 10^{-3} Pa s, respectively. The lattice spacing of the fluid field is chosen at 0.1 μm.

5.3. Coarse-grained models for NMC622, super P, and binder

To capture the dynamic motion of NMC622, Super P, and Binder, a Large-scale Atomic/Molecular Massively Parallel Simulator (LAMMPS) [39] is employed to perform all simulations. As shown in Fig. S12 (A), the NMC622 is described as a spherical particle. The diameter of NMC622 is 3.5 μm, with a surface area of 38.4845 μm^2 and a volume of 22.449 μm^3 per particle, which corresponds to the experimental measurement. NMC622 is then uniformly discretized into a series of points with a triangular network of 3558 vertices and 7112 elements, similar to our red blood cell model [31]. The mechanical behaviors of the coarse-grained NMC622 spherical particles are dominated by the in-plane stretching and out-of-plane bending. In addition, constraints are applied to keep the area and volume of individual NMC622 spherical particle constant during the simulation. The potential energy function of a single NMC622 particle is expressed as $U(x_i) = U_{stretching} + U_{bending} + U_{area} + U_{volume}$. $U_{stretching}$ is the in-plane stretch resistance of NMC622 particles. $U_{bending}$ is bending resistance. $U_{area}$and U_{volume} are used to govern the total area and volume conservation, corresponding to the area and volume incompressibility.

The binder is modeled as a polymer chain with unceasingly connected beads. As shown in Fig. S12 (B), binders are considered as a series of coarse-grained polymer chains where each chain has a length of 22 μm and 147 beads. All beads of the polymer chain are sequentially connected by harmonic springs, where a harmonic bending potential is implemented among three consecutive beads to govern the binder stiffness. The bond stiffness is set high enough to keep the numerical stability and chain inextensibility, and the bond stiffness, k_{sp}, is set high enough. The bending stiffness, k_b, is used to ensure the binder stiffness according to their persistent length. Here, according to our previous studies [38], the bending stiffness is set to 50 k_BT.

As shown in Fig. S12 (C), Super P is described as a point particle. Each particle has a diameter of 40 nm. In addition to the above potentials, inter-molecular interactions between NMC622 particles are described as the Morse potential [40,41] with the functional form$U_{morse} = D_0[e^{-2\beta(r-r_0)} - 2e^{-2\beta(r-r_0)}]$, $r < r_c$. D_0 is the energy well depth; β is the width of the potential well, r is the distance between two particles, r_0 is the equilibrium distance, and r_c is the cutoff distance. A short-range and pure repulsive Lennard−Jones potential is also used to prevent overlapping between NMC622 particles. The inter-molecular interactions between super P particles or molecular chains are described as having the same LJ potential. The inter-molecular interaction between NMC 622 particles and super P particles, NMC 622 particles and binders, and super P particles and binders are also described by LJ potential. Our previous work has calibrated all these potential parameters [38]. All these simulations and physical parameters are summarized in Table S2.

5.4. Coupling scheme

A recently developed package by Ye and co-workers, namely Open FSI [42], is employed to characterize the fluid-structure interaction (FSI) using immersed boundary (IB) method to couple LBM with LAMMPS [43–45]. The fluid lattices and NMC622 particles are described by Eulerian and Lagrangian mesh points, respectively. The Eulerian resolution was 4 mesh points per micrometer in all directions. There were about 14 Eulerian points across one NMC622 diameter, which can sufficiently capture the deformation and motion of NMC [35,46]. The coupling between Eulerian and Lagrangian mesh points is fulfilled by

interpolating their velocities and forces. This coupling scheme has been validated by our previous work [38].

5.5. Shear flow behavior and viscosity calculation

Based on the final equilibrium configurations of the three methods, we first describe the shear flow behavior of the ink during the process of printing. The shear flow is driven along the y-direction by moving the z-top flat plate with the same y-direction velocities, calculated from the shear rate values with the formula $v_{top} = shear\ rate \times channel\ height$. Here, a shear rate of 20 s^{-1} is employed to represent the experimental measurement during the process of printing. With regard to the viscosity, the traditional method to calculate the viscosity is to implement a flow velocity at the top, which can be expressed as, $\mu = Fy/Au$, where μ is the viscosity, y is the thickness normal to the velocity direction, A is the cross-sectional area, u is the applied flow velocity at the top, and F is the force on the top. However, this traditional method is difficult to extract the force (F) on the top for the current OpenFSI package. Here, an alternative approach (Fig. S11) is employed to calculate the viscosity in a rectangular channel, which has been verified by experiment and theory [33]. Within this method, the viscosity is written as, $\mu = \tau_w/\dot{\gamma}_w$, where μ is the viscosity, τ_w is the shear stress related to the pressure and geometry parameters, and γ_w is the shear rate associated with the apparent shear rate, volumetric flow, geometry parameters and the empirical model.

To evaluate the viscosity by using the alternative approach, as shown in Fig. S12 (D), the whole channel is divided into three regions along the y direction, named F-region, buffer, and C-region, respectively. In order to generate the Poiseuille flow through the channel, a driving constant pressure gradient across the channel is exerted on the system by applying a driving force on particles in F-region. A more significant force corresponds to a greater pressure gradient. The exerted lateral force [47–49], to the particles is proportional to pressure drop as described by $\Delta P \propto NF/A$, where ΔP is the pressure drop, A is the cross-sectional area perpendicular to the applied force, and N is the number of particles at the inlet region calculating at each time step and averaging over the total simulation time. The effect of pressure gradient on transport behavior is examined by changing the force range from 1.602×10^{-11} to 6.408×10^{-9} N. All simulations are performed to simulate mass transport for 4 s, which is long enough to obtain a steady-state flow, and all calculations are executed in the C-region. All snapshots derived from the simulations are rendered using Visual Molecular Dynamics (VMD) software [50].

CRediT authorship contribution statement

Ying Wang: Methodology, Writing – review & editing, Investigation. **Jinlong He:** Software, Writing – review & editing. **Daxian Cao:** Methodology, Investigation, Writing – review & editing. **Ercan Cakmak:** Methodology, Investigation. **Xianhui Zhao:** Methodology, Investigation. **Qingliu Wu:** Supervision, Funding acquisition. **Yuyue Zhao:** Methodology. **Haoze Ren:** Methodology. **Xiao Sun:** Methodology. **Ying Li:** Investigation, Supervision. **Hongli Zhu:** Conceptualization, Writing – review & editing, Investigation, Supervision.

Declaration of Competing Interest

None.

Acknowledgment

This work is supported by the U. S. Department of Energy's Office of Energy Efficiency and Renewable Energy (EERE) under the Advanced Manufacturing Office, award number DE-EE0009111. The authors appreciate Nanoramic Laboratories (Boston, MA, 02210, USA) for providing multi-crystalized NMC 622 for this study. The authors thank Northeastern University Center for Renewable Energy Technology (NUCRET) for the use of SEM. This manuscript has been authored by UT-Battelle, LLC, under contract DE-AC05-00OR22725 with the US Department of Energy (DOE). The US government retains and the publisher, by accepting the article for publication, acknowledges that the US government retains a nonexclusive, paid-up, irrevocable, worldwide license to publish or reproduce the published form of this manuscript, or allow others to do so, for US government purposes. DOE will provide public access to these results of federally sponsored research in accordance with the DOE Public Access Plan (http://energy.gov/downloads/doe-public-access-plan). Y.L. would like to thank the support from the US National Science Foundation under Grants 1755779 and 1762661, as well as 3M's Non-Tenured Faculty Award.

Supplementary materials

Supplementary material associated with this article can be found, in the online version, at doi:10.1016/j.ensm.2022.11.025.

References

[1] Y. Liu, Y. Zhu, Y. Cui, Challenges and opportunities towards fast-charging battery materials, Nat. Energy 4 (7) (2019) 540–550.
[2] H. Chen, et al., Tortuosity effects in lithium-metal host anodes, Joule 4 (4) (2020) 938–952.
[3] D.P. Singh, et al., Facile micro templating LiFePO4 electrodes for high performance Li-Ion batteries, Adv. Energy Mater. 3 (5) (2013) 572–578.
[4] R. Xiong, et al., Scalable manufacture of high-performance battery electrodes enabled by a template-free method, Small Methods 5 (6) (2021), 2100280.
[5] J. Billaud, et al., Magnetically aligned graphite electrodes for high-rate performance Li-ion batteries, Nat. Energy 1 (8) (2016) 1–6.
[6] J. Sander, et al., High-performance battery electrodes via magnetic templating, Nat. Energy 1 (8) (2016) 1–7.
[7] C.J. Bae, et al., Design of battery electrodes with dual-scale porosity to minimize tortuosity and maximize performance, Adv. Mater. 25 (9) (2013) 1254–1258.
[8] S. Behr, et al., Highly-structured, additive-free lithium-ion cathodes by freeze-casting technology, Ceram. Forum Int (2015).
[9] L.L. Lu, et al., Wood-inspired high-performance ultrathick bulk battery electrodes, Adv. Mater. 30 (20) (2018), 1706745.
[10] B. Shi, et al., Low tortuous, highly conductive, and high-areal-capacity battery electrodes enabled by through-thickness aligned carbon fiber framework, Nano Lett. 20 (7) (2020) 5504–5512.
[11] Y. Liu, et al., Architecturing hierarchical function layers on self-assembled viral templates as 3D nano-array electrodes for integrated Li-ion microbatteries, Nano Lett. 13 (1) (2013) 293–300.
[12] Z. Wang, et al., Development of MnO2 cathode inks for flexographically printed rechargeable zinc-based battery, J. Power Sources 268 (2014) 246–254.
[13] Y. Wang, et al., Large-scale manufacturing of pattern-integrated paper Li-Ion microbatteries through roll-to-roll flexographic printing, Adv. Mater. Technol. (2022), 2200303.
[14] H.W. Vollmann, New technologies for the filmless manufacture of printing forms, Angew. Chem. Int. Ed Engl. 19 (2) (1980) 99–110.
[15] C. Costa, R. Gonçalves, S. Lanceros-Méndez, Recent advances and future challenges in printed batteries, Energy Storage Mater. 28 (2020) 216–234.
[16] X. Zhang, et al., Extending cycling life of lithium–oxygen batteries based on novel catalytic nanofiber membrane and controllable screen-printed method, J. Mater. Chem. A 6 (43) (2018) 21458–21467.
[17] T. Syrový, et al., Cathode material for lithium ion accumulators prepared by screen printing for Smart Textile applications, J. Power Sources 309 (2016) 192–201.
[18] O. El Baradai, et al., Use of cellulose nanofibers as an electrode binder for lithium ion battery screen printing on a paper separator, Nanomaterials 8 (12) (2018) 982.
[19] R. Sousa, et al., High performance screen printable lithium-ion battery cathode ink based on C-LiFePO4, Electrochim. Acta 196 (2016) 92–100.
[20] A. Gören, et al., High performance screen-printed electrodes prepared by a green solvent approach for lithium-ion batteries, J. Power Sources 334 (2016) 65–77.
[21] Y. Liu, et al., Current and future lithium-ion battery manufacturing, Iscience (2021), 102332.
[22] C.P. Hsu, et al., Effect of polymer binders in screen printing technique of silver pastes, J. Polym. Res. 20 (10) (2013) 1–8.
[23] M. Hatala, et al., The effect of the ink composition on the performance of carbon-based conductive screen printing inks, J. Mater. Sci. Mater. Electron. 30 (2) (2019) 1034–1044.
[24] M.R. Somalu, et al., Screen-printing inks for the fabrication of solid oxide fuel cell films: a review, Renew. Sustain. Energy Rev. 75 (2017) 426–439.
[25] D. Marani, et al., Influence of hydroxyl content of binders on rheological properties of cerium–gadolinium oxide (CGO) screen printing inks, J. Eur. Ceram. Soc. 35 (5) (2015) 1495–1504.
[26] F. Zou, A. Manthiram, A review of the design of advanced binders for high-performance batteries, Adv. Energy Mater. 10 (45) (2020), 2002508.

[27] Y. Zhang, et al., Ink formulation, scalable applications and challenging perspectives of screen printing for emerging printed microelectronics, J. Energy Chem. (2021).
[28] G. Hu, et al., Functional inks and printing of two-dimensional materials, Chem. Soc. Rev. 47 (9) (2018) 3265–3300.
[29] D. Cao, et al., Amphipathic binder integrating ultrathin and highly ion-conductive sulfide membrane for cell-level high-energy-density all-solid-state batteries, Adv. Mater. (2021), 2105505.
[30] Q. Wang, et al., Origin of structural evolution in capacity degradation for overcharged NMC622 via operando coupled investigation, ACS Appl. Mater. Interfaces 9 (29) (2017) 24731–24742.
[31] H. Ye, Z. Shen, Y. Li, Computational modeling of magnetic particle margination within blood flow through LAMMPS, Comput. Mech. 62 (3) (2018) 457–476.
[32] H. Ye, Z. Shen, Y. Li, Interplay of deformability and adhesion on localization of elastic micro-particles in blood flow, J. Fluid Mech. 861 (2019) 55–87.
[33] Y. Son, Determination of shear viscosity and shear rate from pressure drop and flow rate relationship in a rectangular channel, Polymer 48 (2) (2007) 632–637.
[34] S. Chen, G.D. Doolen, Lattice Boltzmann method for fluid flows, Annu. Rev. Fluid Mech. 30 (1) (1998) 329–364.
[35] R.M. MacMeccan, et al., Simulating deformable particle suspensions using a coupled lattice-Boltzmann and finite-element method, J. Fluid Mech. 618 (2009) 13–39.
[36] H. Ye, et al., Dynamics of a nonspherical capsule in general flow, Comput. Fluids 134-135 (2016) 31–40.
[37] J. Zhang, P.C. Johnson, A.S. Popel, Red blood cell aggregation and dissociation in shear flows simulated by lattice Boltzmann method, J. Biomech. 41 (1) (2008) 47–55.
[38] H. Ye, et al., Anomalous vascular dynamics of nanoworms within blood flow, ACS Biomater. Sci. Eng. 4 (1) (2018) 66–77.
[39] S. Plimpton, Fast parallel algorithms for short-range molecular dynamics, J. Comput. Phys. 117 (1) (1995) 1–19.
[40] D.A. Fedosov, et al., Predicting human blood viscosity in silico, Proc. Natl. Acad. Sci. 108 (29) (2011) 11772.
[41] J. Tan, A. Thomas, Y. Liu, Influence of red blood cells on nanoparticle targeted delivery in microcirculation, Soft Matter. 8 (6) (2012) 1934–1946.
[42] H. Ye, et al., OpenFSI: a highly efficient and portable fluid–structure simulation package based on immersed-boundary method, Comput. Phys. Commun. 256 (2020), 107463.
[43] T. Krüger, F. Varnik, D. Raabe, Efficient and accurate simulations of deformable particles immersed in a fluid using a combined immersed boundary lattice Boltzmann finite element method, Comput. Math. Appl. 61 (12) (2011) 3485–3505.
[44] C.S. Peskin, The immersed boundary method, Acta Numer. 11 (2003) 479–517.
[45] H. Ye, et al., Two tandem flexible loops in a viscous flow, Phys. Fluids 29 (2) (2017), 021902.
[46] K. Vahidkhah, P. Bagchi, Microparticle shape effects on margination, near-wall dynamics and adhesion in three-dimensional simulation of red blood cell suspension, Soft Matter. 11 (2015).
[47] F. Zhu, E. Tajkhorshid, K. Schulten, Pressure-induced water transport in membrane channels studied by molecular dynamics, Biophys. J. 83 (1) (2002) 154–160.
[48] M. Kazemi, A. Takbiri-Borujeni, Non-equilibrium molecular dynamics simulation of gas flow in organic nanochannels, J. Nat. Gas Sci. Eng. 33 (2016) 1087–1094.
[49] R. Carr, et al., Modeling pressure-driven transport of proteins through a nanochannel, IEEE Trans. Nanotechnol. 10 (1) (2011) 75–82.
[50] W. Humphrey, A. Dalke, K. Schulten, VMD: visual molecular dynamics, J. Mol. Gr. 14 (1) (1996) 33–38.